Influence of Entrainment on Centimeter-Scale Cloud Microphysics in Marine Stratocumulus Clouds Observed during CSET

INYEOB LA,[a] SEONG SOO YUM,[a] JAE MIN YEOM,[b] AND RAYMOND A. SHAW[b]

[a] *Department of Atmospheric Sciences, Yonsei University, Seoul, South Korea*
[b] *Department of Physics, Michigan Technological University, Houghton, Michigan*

(Manuscript received 12 January 2022, in final form 14 June 2022)

ABSTRACT: Cloud microphysical relationships observed during the Cloud System Evolution in the Trades (CSET) campaign held between Northern California and Hawaii were analyzed to study the effects of entrainment and subsequent mixing of free-tropospheric and cloudy air on cloud microphysical properties of marine stratocumulus clouds. The data measured by Holographic Detector for Clouds (HOLODEC) were extensively used because they could provide the 3D positions and sizes of droplets within sample volume on the centimeter scale, making it possible to explore the 3D spatial distribution of droplets, which has not been possible for conventional cloud probes. This study focused on analyzing the 3D spatial distribution of droplets and visual traits of inhomogeneous mixing and on quantifying the relationship between 3D spatial distributions and traits of inhomogeneous mixing. Two types of spatial distributions are compared. The first is measured droplet spatial distribution and the second type is generated randomly distributed droplets using the Monte Carlo approach, that is, to analyze whether or not clustering is strong enough to classify as a clustered distribution for a hologram. The difference between the two types of spatial distributions depends on whether they are affected by entrainment and mixing. The holograms observed near the cloud top, where the effects of entrainment and mixing would be immediate, showed relatively high confidence in the significance test for spatially clustered populations of droplets. Moreover, spatially clustered holograms appeared to exhibit stronger visual traits of inhomogeneous mixing than perfectly randomly distributed holograms only when observed near the cloud top. On the other hand, these characteristics did not appear for holograms observed deeper into the cloud where the effects of entrainment and mixing would be reduced. Such 3D structural characteristics of droplet distributions seem to be consistent with vertical circulation mixing.

KEYWORDS: Cloud droplets; Cloud microphysics; Drop size distribution

1. Introduction

Rain is often observed within 30 min after cloud formation (Rogers and Yau 1989), but there is no clear explanation for how cloud droplets grow to become raindrops in such a short time. It is challenging to explain the growth of cloud droplets in the approximately 20–40 μm diameter range, where neither the growth by condensation nor by collision–coalescence is effective. Extensive studies have been conducted over the past few decades to understand this problem (e.g., Baker et al. 1980; Jonas 1996; Pruppacher and Klett 1997; Vaillancourt and Yau 2000; Shaw et al. 2002; McGraw and Liu 2004; Grabowski and Wang 2009; Lehmann et al. 2009; Devenish et al. 2012; Yum et al. 2015; Yeom et al. 2019; Hoffmann et al. 2019; Desai et al. 2019; Lu et al. 2020). Turbulent entrainment–mixing between ambient dry air and cloudy air is one of the ideas that may solve warm rain initiation problems that are not yet fully understood. Turbulent entrainment and mixing scenarios are classified into two types: homogeneous and inhomogeneous mixing. In the case of homogeneous mixing, it is considered that the time scales of turbulent homogenization are much shorter than the time scales of droplet evaporation. As a result, all droplets experience the same subsaturation, eventually reducing both droplet sizes and number concentration by dilution (Warner 1973). If the opposite is the case, inhomogeneous mixing may occur. In this scenario, the droplets adjacent to the entrained air evaporate completely but the other droplets in the mixed parcel maintain their original sizes (Baker et al. 1980). If this parcel ascends, droplets can grow faster than those in undiluted adiabatic parcel because with the reduced concentration they would have less competition for water vapor than those in the undiluted cloudy air (Yang et al. 2016). To examine which mixing scenario is relevant to real clouds, several studies analyzed the microphysical relationship between droplet number concentration (or liquid water content) and droplet size observed in clouds (e.g., Pawlowska et al. 2000; Yum and Hudson 2001; Burnet and Brenguier 2007; Lu et al. 2011; Yum et al. 2015; Yeom et al. 2017).

From the spatial structure point of view, the entrainment–mixing process could induce spatial clustering of cloud droplets. Baker (1992) studied the effect of entrainment and mixing on the spatial clustering of cloud droplets as a new observational approach to examine whether or not cloud droplets were located perfectly randomly in space, instead of analyzing entrainment and mixing indirectly by interpreting measured droplet microphysical relationships. However, Baker (1992) discussed that the explanations for spatial clustering at small scales between 0.5 and 5 cm remain speculative and unclear. Meanwhile, Shaw (2003) argued that spatial clustering at centimeter scales and below could also be caused by

Supplemental information related to this paper is available at the Journals Online website: https://doi.org/10.1175/JAS-D-22-0005.s1.

Corresponding author: Prof. Seong Soo Yum, ssyum@yonsei.ac.kr

DOI: 10.1175/JAS-D-22-0005.1

strong fluid accelerations leading to preferential concentration, and more recent observation (Larsen et al. 2018) suggested that inertial-droplet clustering was dominant in the range of approximately 0.1–0.5 cm but not at larger scales. On the other hand, Dodson and Small Griswold (2019) showed that spatial clustering not only at meter scales but also at centimeter scales was enhanced in the edges of cumulus cloud compared to the cloud center and suggested that the entrainment occurring at cloud edges could lead to spatial clustering at centimeter scales.

The effects of entrainment and mixing on droplet spatial structure at centimeter scales within the observational framework for homogeneous and inhomogeneous mixing are not studied yet. Theoretically, in the course of inhomogeneous mixing, spatial clustering of cloud droplets could occur. Because the time scale for turbulent mixing is much slower than the time scale for evaporation of cloud droplets, some droplets might evaporate completely in the sections that are in immediate contact with the entrained subsaturated air but in other sections droplet evaporation would be limited, which would induce nonuniformly populated droplet spatial distribution. That is, some parts are relatively sparsely populated due to complete evaporation of droplets but in other parts droplet population is largely maintained, and therefore looks clustered when compared to those in relatively sparsely populated sections. On the other hand, in the course of homogeneous mixing, the mixing time scale is much shorter than the evaporation time scale. Therefore, evaporation occurs uniformly after the entrained air is completely mixed with cloudy air, which implies that if droplets were initially randomly distributed, such droplet distribution pattern would have been preserved.

Several studies (Uhlig et al. 1998; Beals 2013; Beals et al. 2015) analyzed the 3D spatial distribution of droplets to quantify spatial clustering. Uhlig et al. (1998) compared the first and second neighbor distances between cloud droplets from six holograms measured by Holographic Droplet and Aerosol Recording system with the theoretical Poisson distribution. Beals (2013) and Beals et al. (2015) also quantified spatial clustering using the 1st-nearest-neighbor distance recorded by the Holographic Detector for Clouds (HOLODEC). We use the HOLODEC data observed during the Cloud System Evolution in the Trades (CSET) campaign. The main advantage of HOLODEC is to provide the 3D positions and sizes of droplets within ~13 cm^3 sample volume with a temporal resolution of 3.3 Hz. Conventional instruments (e.g., Cloud Droplet Probe or Forward Scattering Spectrometer Probe) have been called as 1D instruments because they continuously measure a single droplet within the sample area similar to the area of a needle (~0.1–1 mm^2). That is, HOLODEC gives us an opportunity to explore the 3D spatial distribution of droplets, which has not been possible for the conventional cloud probes. This study focuses on analyzing the 3D spatial distribution of droplets along with the kth (k is the rank number of the nearest neighbors) nearest neighbor as well as the 1st-nearest-neighbor distance plot and quantifying the relationship between 3D spatial distribution of droplets and visual traits of inhomogeneous mixing.

This paper is organized as follows. In section 2, the principal instruments and data processing methods are explained. Section 3 explains the analysis method and presents the results of 3D spatial distribution of droplets along with the kth-nearest-neighbor distance plot. Section 4 shows the results of the analysis of inhomogeneous mixing traits in relation to spatial clustering. A relevant discussion is made on spatial clustering and traits of inhomogeneous mixing in section 5, and the summary and conclusions are given in section 6.

2. Data

The data used in this study were collected during the Cloud System Evolution in the Trades (CSET) campaign held off between Northern California and Hawaii from 1 July to 15 August 2015. A suite of instruments was installed onboard the National Science Foundation Gulfstream-V (G-V) research aircraft as described in detail by Albrecht et al. (2019). The airborne instruments included the HOLODEC, cloud droplet probe (CDP), two-dimensional optical array cloud probe (2DC), King probe, and HIAPER Cloud Radar (HCR). In this study, we analyze the data from the two research flights, RF02 and RF10.

HOLODEC takes snapshots of cloud droplets of the diameters from about 6 μm up to a millimeter range in an approximately 13 cm^3 sample volume at a rate of 3.3 Hz. Glienke et al. (2017) demonstrated that the droplet size distributions measured by HOLODEC were consistent with those collected with CDP and 2DC combined. However, HOLODEC shows the best detectability for the droplets of diameter larger than 10 μm (Glienke et al. 2017; Larsen et al. 2018; Glienke et al. 2020). We focus on analyzing observed droplets larger than 10 μm to ensure that only trustworthy HOLODEC data are used. Moreover, droplet detection nonuniformity (meaning that the sample volume has regions with slightly higher or lower detectability) could be a source of spatial clustering in the original sample volume of approximately 1 cm × 1 cm × 13 cm (Beals 2013; Larsen et al. 2018; Glienke et al. 2020). So, the sample volume of 0.6 cm × 0.6 cm × 10 cm (3.6 cm^3) in the central part, where HOLODEC retains approximately uniform sensitivity, is examined for analysis as Larsen et al. (2018) did.

The cloud samples are defined with the criterion of minimum 100 droplets per 3.6 cm^3 volume (Larsen et al. 2018). The aircraft data observed only when the non-drizzling clouds criterion was satisfied are analyzed to avoid the impact of the collision–coalescence process on cloud microphysics. The criterion for non-drizzling clouds is that in-cloud mean drizzle water content of HOLODEC measurements (radius > 25 μm) is smaller than 0.005 g m^{-3}. The cloud microphysical variables, such as liquid water content (LWC), mean volume diameter (D_v), and number concentration (N_c) are examined, and spatial clustering and visual traits of inhomogeneous mixing are quantified for the cloud samples that satisfy the above criteria.

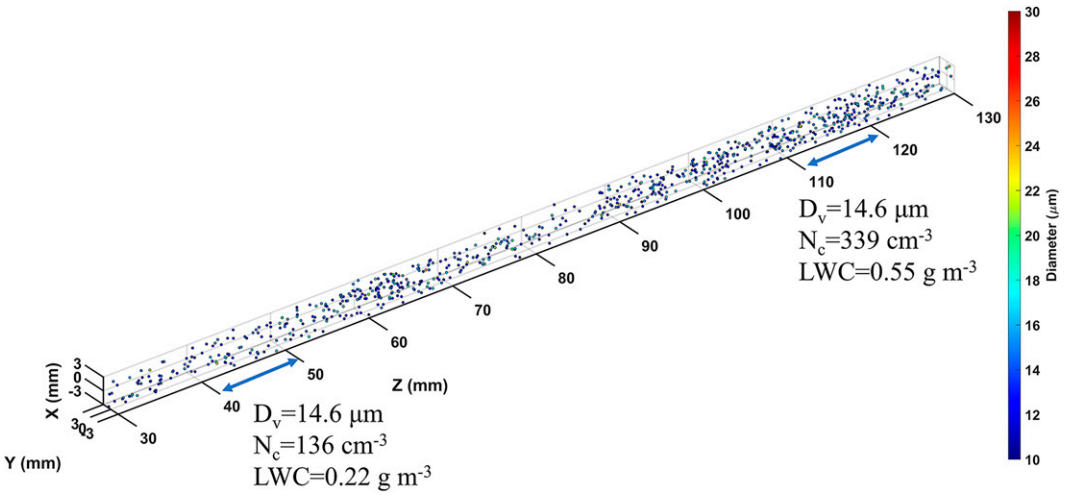

FIG. 1. A snapshot of a clustered distribution of cloud droplets measured by the HOLODEC instrument.

3. Spatial clustering

To characterize spatial clustering, droplet spatial distributions of HOLODEC measurements are presented and then those of Monte Carlo calculations are compared. Figure 1 shows an example of spatially clustered distribution of cloud droplets observed from HOLODEC. There are relatively fewer cloud droplets in the section from 30 to 90 mm in z coordinate than in other sections. In this study these droplet distributions are referred to as "clustered" (i.e., spatially correlated; Shaw (2003)) and they are quantified using the kth-nearest-neighbor distances calculated from 3D droplet positions recorded by the HOLODEC. Figures 2a and 2b show the plots of sorted distance to the 1st- and 65th-nearest cloud droplets, respectively, for the distribution shown in Fig. 1. That is, for each cloud droplet, the distances to the 1st- and 65th-nearest droplets are identified and sorted by the distance values. Shown together are the purple, red, and yellow lines that represent the 90th percentile, median, and 10th percentile [hereafter $d_{90,i}(k)$, $d_{50,i}(k)$, and $d_{10,i}(k)$, respectively] of the 1st- and 65th-nearest distances of the ith points sorted by distance for the 10 000 Monte Carlo simulations. The total count of cloud droplets is 777 in Fig. 1 and therefore the total number of points in the Monte Carlo simulations is set to be equal to this number. As illustrated in Fig. 2c, when droplet clustering is obvious, there would be droplets at a farther distance or a closer distance than the randomly distributed droplets. The following expression calculates spatial clustering (SC) as a measure to quantify these differences in distance for the kth-nearest droplet:

$$\mathrm{SC}(k) = \sqrt{\frac{\sum_{i=1}^{n} \{[x_i(k) - d_{50,i}(k)]/y_i(k)\}^2}{n}}. \qquad (1)$$

Here $y_i(k)$ is the measure of the distribution breadth as

$$y_i(k) = \begin{cases} d_{90,i}(k) - d_{50,i}(k) & \text{if } x_i(k) > d_{50,i}(k) \\ d_{50,i}(k) - d_{10,i}(k) & \text{if } x_i(k) < d_{50,i}(k) \end{cases}, \qquad (2)$$

where $x_i(k)$ is the kth-nearest distance of the ith cloud droplet sorted by distance and n is the total number of cloud droplets in the sample volume of 3.6 cm^3. Figure S1 in the online supplemental material in the Supporting Information shows that y_i is characteristically different for different k values. Equation (1) describes how different the observed distribution is from the perfectly random distribution. Although cloud droplets are not perfectly randomly distributed in Fig. 1, SC(1) for the 1st-nearest neighbor is approximately 0.5, meaning that the observed distribution is close to a perfect random distribution, but SC(65) for the 65th-nearest neighbor is approximately 7.1. It implies that spatial clustering varies with the k value. Therefore, Eq. (1) was calculated not only for the 1st-nearest neighbor but also for several other kth-nearest neighbors.

SC(k) from the perfect random distributions is used to decide whether there is a statistically significant deviation from perfect randomness for each hologram sample. The kth distances of the perfectly randomly distributed points of the Monte Carlo simulations calculated above are substituted into $x_i(k)$ in Eq. (1) and we calculate the SC(k) for each of all 10 000 Monte Carlo simulations. And then, the observed SC(k) [$\mathrm{SC_{obs}}(k)$] and the 99.9th percentile of the 10 000 simulated SC(k) [$\mathrm{SC_{99.9}}(k)$] are compared. For example, if $\mathrm{SC_{obs}}(1)$ is 0.6 but $\mathrm{SC_{99.9}}(1)$ is 1.8, then the ratio, which indicates relative spatial clustering (RC), is 0.33 [$\mathrm{RC}(1) = \mathrm{SC_{obs}}(1)/\mathrm{SC_{99.9}}(1) = 0.33$). Figure 3 shows that RC varies with k for the hologram shown in Fig. 1. If the maximum of RC(k) ($\mathrm{RC_{max}}$) for a hologram is greater than 1, then it can be said that the hologram has statistically very significant clustering (i.e., p value is lower than 0.001). In Fig. 3, $\mathrm{RC_{max}}$ is 3.4, implying that the hologram shown in Fig. 1 shows statistically significant clustering. On the other hand, for the hologram shown in Fig. 4, an example of seemingly perfectly random spatial distribution, $\mathrm{RC_{max}}$ value

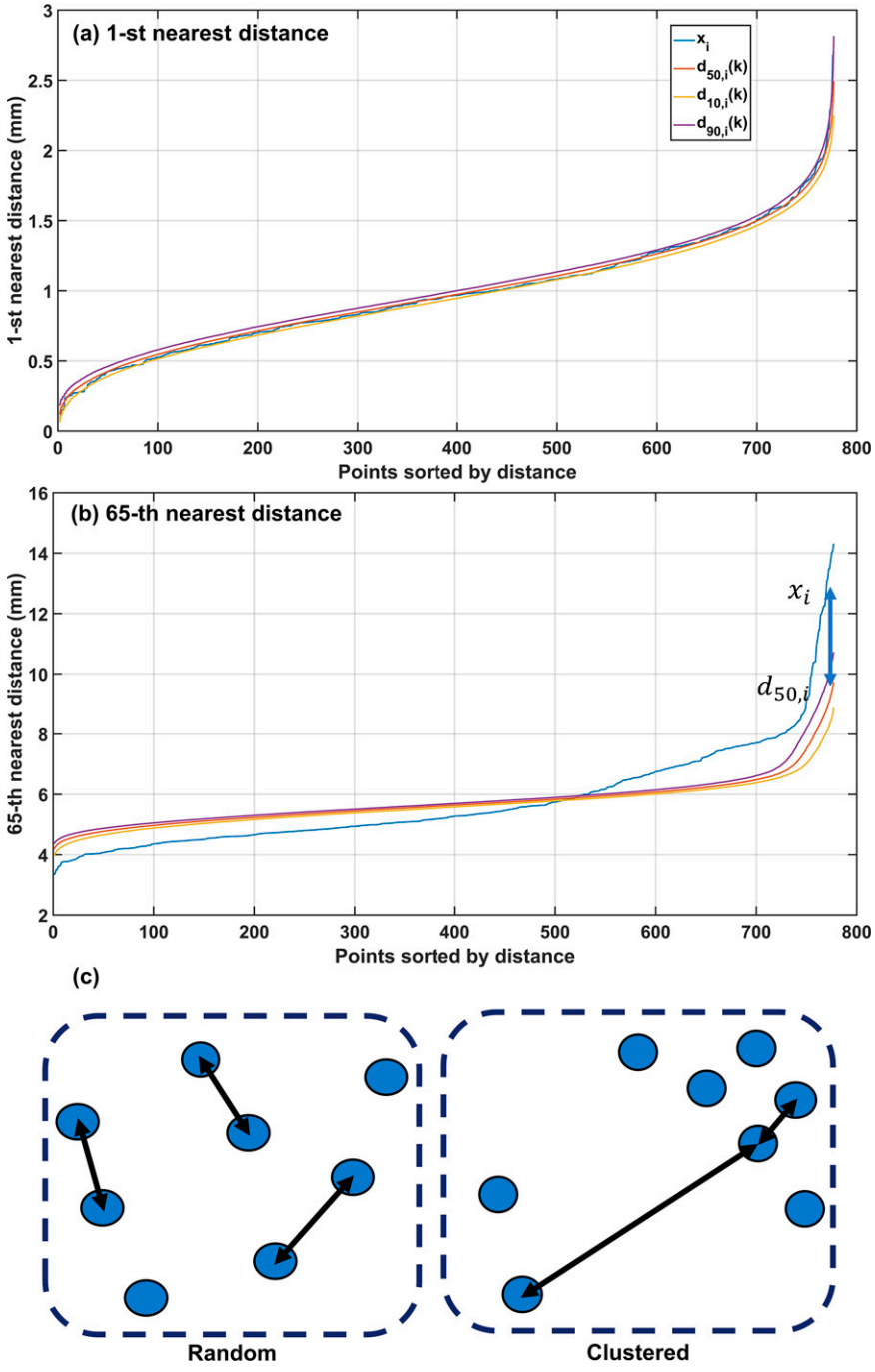

FIG. 2. (a) The 1st- and (b) 65th-nearest-distance plot. The blue lines are the observed 1st- and 65th-nearest distances. The purple, red, and yellow lines represent $d_{90,i}(k)$, $d_{50,i}(k)$, and $d_{10,i}(k)$, respectively, which are from 10 000 Monte Carlo simulations, the meaning of which is explained in the text. (c) Schematic diagram of (left) random and (right) clustered distribution of droplets.

is 0.9, which is smaller than 1, indicating that clustering was not strong enough to classify it as a clustered distribution for this hologram. We call it a random distribution for lack of a better term.

The next step is to analyze the droplet distributions in spatially clustered holograms and randomly distributed holograms, within the observational framework of homogeneous and inhomogeneous mixing. For that, the visual traits of

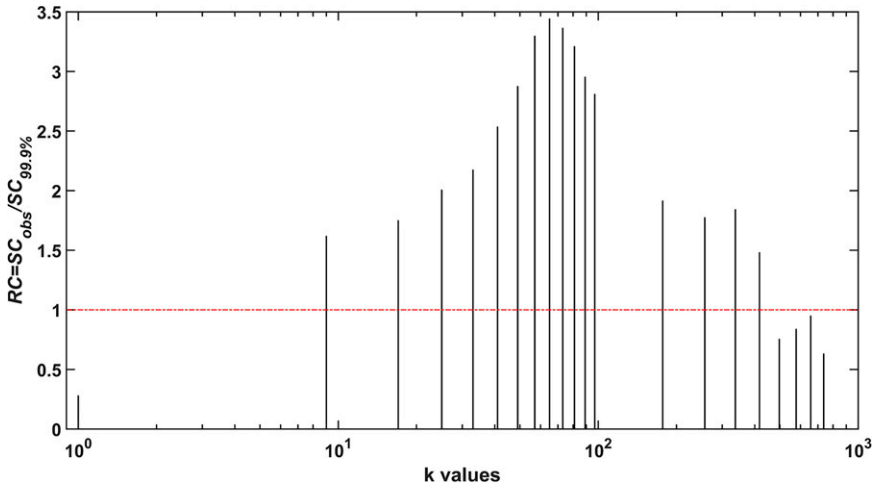

FIG. 3. RC(k) for the hologram shown in Fig. 1. The dashed red line is RC(k) value of 1.

inhomogeneous mixing are compared between the spatially clustered and random holograms as described in the next section.

4. Visual traits of inhomogeneous mixing

During the flight RF02 on 7 July 2015, holograms were observed at various cloud altitudes. Figure 5 shows that the holograms were observed at approximately 40 m distance from the cloud top near the time of entry into the cloud (Fig. 5a) and approximately 50 m below the cloud top near the time of exiting the cloud (Fig. 5b). In the middle of horizontal penetration, there was a period when detectable cloud radar echo was produced (Fig. 5c), implying that the distance from the cloud top was deeper than 100 m for this period since the minimum detection range of cloud radar is approximately 100 m cloud depth. It means that the distance from the cloud top was not uniform for this penetration. To note is the variation of RC_{max} during this penetration (Fig. 5c). The spatially clustered holograms ($RC_{max} > 1$) are more frequently observed when the aircraft is relatively closer to the cloud top than when relatively deeper into the cloud. There are 895 holograms observed near the cloud top regions that exclude the region when cloud radar echo existed and 60 of them are spatially clustered holograms. There are 1014 holograms observed when the aircraft is relatively deeper into the cloud where cloud radar echo existed, and only 32 of them are spatially clustered holograms. Moreover, holograms with relatively higher confidence for spatial clustering ($RC_{max} > 1.5$) are mostly observed when the aircraft is near the cloud top. The causes of the observed spatial clustering are discussed in more detail in section 5.

As mentioned in the introduction, it is expected that spatially clustered holograms would show visual traits of inhomogeneous mixing. This section focuses mainly on investigating visual traits of inhomogeneous mixing at the centimeter-scale, especially in spatially clustered holograms. For example, in Fig. 1, D_v and N_c of the droplets at 110 to 120 mm section in

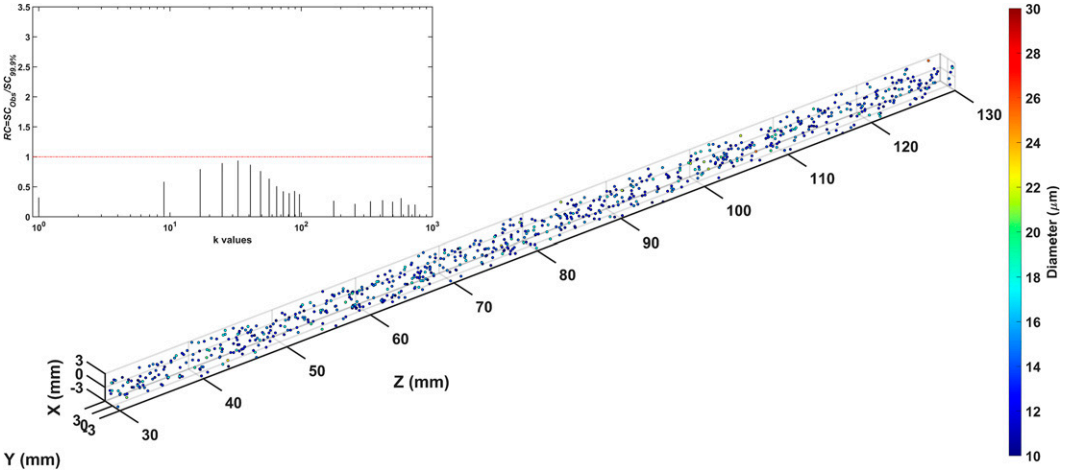

FIG. 4. A snapshot of a randomly distributed cloud droplets, shown together with (top left) RC(k).

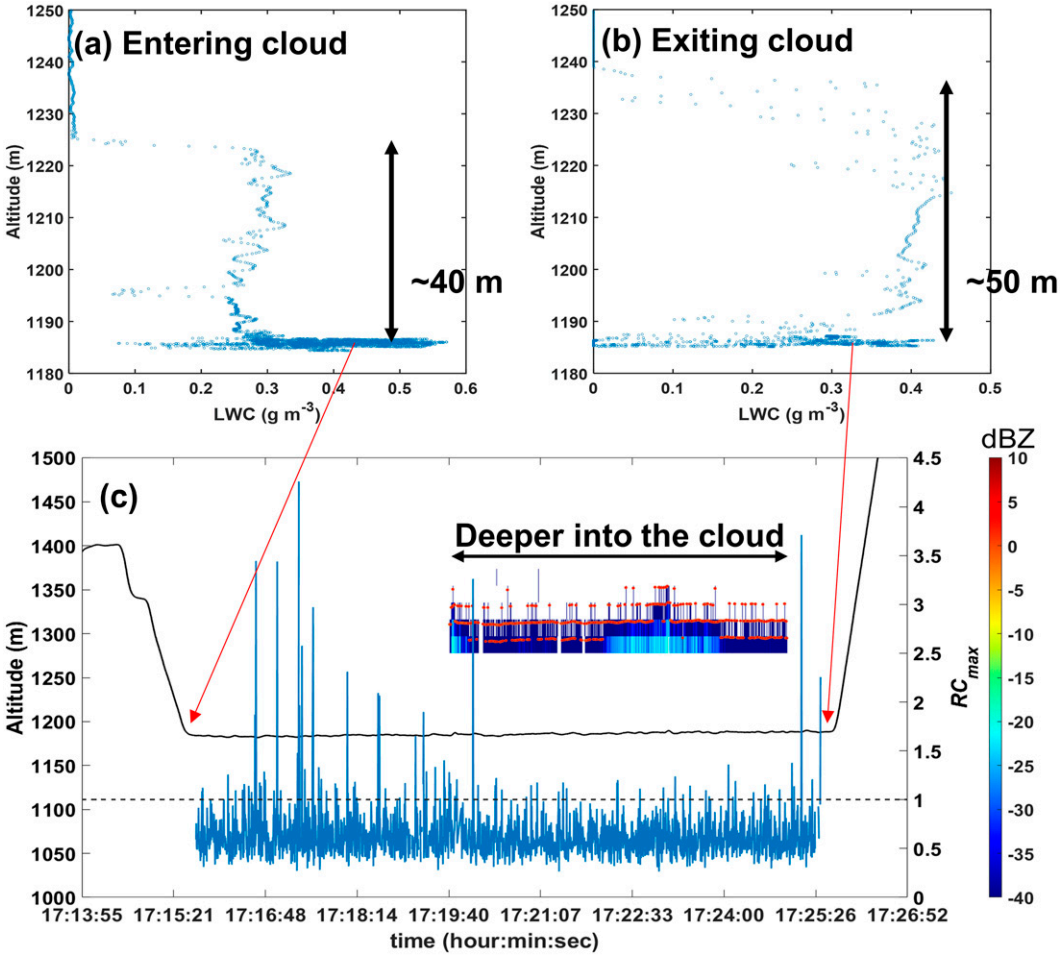

FIG. 5. Vertical profile of 25 Hz LWC measured by King probe when the aircraft (a) enters and (b) exits the cloud, and (c) time variation of RC_{max} (blue line), aircraft altitude (black line), and radar reflectivity factor from the HCR between 1713 and 1726 UTC during RF02 on 7 Jul 2015. Red dots in reflectivity plot indicate the estimated height of cloud top.

z coordinate are ~15 μm and ~340 cm^{-3}, while D_v and N_c at 40–50 mm section in z coordinate are ~15 μm and ~140 cm^{-3}. These microphysical contrasts indicate an inhomogeneous mixing trait. In this way, we attempt to quantify the visual traits of inhomogeneous mixing, based on the degree of homogeneous mixing, obtained by two different methods.

a. Degree of homogeneous mixing in the mixing diagram

At first, we quantify the degree of homogeneous mixing in the mixing diagram, which has been used as a useful tool to investigate mixing characteristics (e.g., Burnet and Brenguier 2007; Lehmann et al. 2009; Yum et al. 2015). The degree of homogeneous mixing, DHM, is the median of the set of ℓ/h values $\{\ell_1/h_1, \ell_2/h_2, \ldots\}$, where ℓ and h are the length along the rectangular hyperbolic lines shown in Fig. 6. In Fig. 6, the adiabatic LWC is defined as $LWC_a = N_a V_a$, where V is the mean volume of cloud droplets and the subscript a indicates the adiabatic value. We assume that the maximum LWC among the LWC values calculated for all subsample volumes in an individual hologram is LWC_a and N and V of this subsample are N_a and V_a, respectively. For example, after dividing the sample volume (6 mm in x axis × 6 mm in y axis × 100 mm in z axis) evenly along the x–y plane so that the length in the z coordinate is 10 mm, the maximum of LWC among the LWCs in 10 subsample volumes (6 mm on the x axis × 6 mm on the y axis ×10 mm on the z axis) is calculated. This would mean that the DHM depends on the subsample length in z coordinate. Here, we calculate DHM(m) for each subsample length in z coordinate between 2 and 20 mm to ensure consistent results, where m is the number of subsamples and it ranges from 5 (for subsample size of 20 mm) to 50 (for subsample size of 2 mm). When DHM(m) is calculated, the ℓ is positive if the data point lies below the red horizontal line shown in Fig. 6, but the ℓ is negative if it lies above the red horizontal line. The homogeneous mixing line is calculated based on the heat and moisture balance equations for isobaric homogeneous mixing at the aircraft observation level. If the volume fraction of the cloudy air is χ, T, and q_l can be expressed as (Yum et al. 2015).

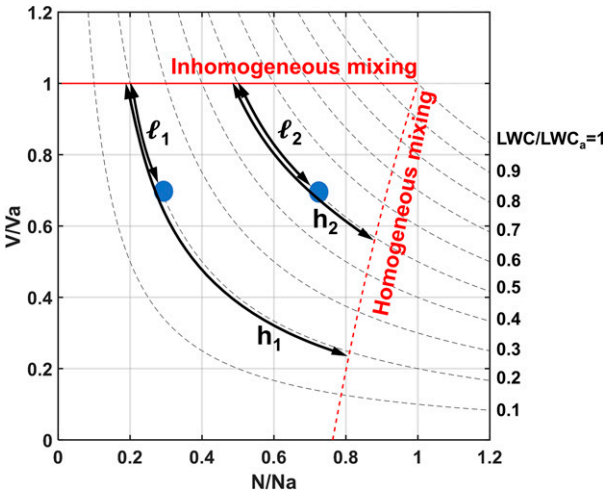

FIG. 6. Definition of homogeneous mixing degree in mixing diagram (adapted from Lu et al. 2014). The horizontal solid red and the dashed red line, respectively, represent inhomogeneous mixing and homogeneous mixing. The exemplary homogeneous mixing line shown here is for RH = 42%. The ℓ and h, respectively, are the length along an isoline of liquid water dilution ratio LWC/LWC$_a$ from the inhomogeneous mixing line to the observed value and to the homogeneous mixing line.

$$T = \left(T_a - T_e - q_{la}\frac{L_v}{C_p}\right)\chi + T_e + q_l\frac{L_v}{C_p}, \tag{3}$$

$$q = \chi[q_{la} - q_{vs}(T_e)\mathrm{RH} + q_{vs}(T_a)] + q_{vs}(T_e)\mathrm{RH} - q_{vs}(T), \tag{4}$$

where L_v and C_p are, respectively, the latent heat of vaporization and the specific heat at constant pressure; T_a, q_{la}, and $q_{vs}(T_a)$ are, respectively, the temperature, liquid water mixing ratio, saturation vapor mixing ratio of the adiabatic cloudy air; and T_e and RH are, respectively, the temperature and the relative humidity of the air above the cloud top. We assume that T_a is the average of seven temperature data collected closest to the time of a hologram, which spans approximately the time of HOLODEC sampling rate, and q_{la} is derived from LWC$_a$. That is, the mixing diagrams are calculated for each subsample length of a hologram. Beals (2013) stated that the discretization of HOLODEC image cause uncertainty in droplet mean volume V of $\pi\sigma_V/(6\sqrt{N})$, where N is the count of droplets and σ_V is the standard deviation of droplet volumes in the sample volume. In this study, the uncertainty in V/V_a for RF02 is calculated and Figure S2 shows the result of the uncertainty in V/V_a. Although the uncertainty in V/V_a is smaller than about 0.1, it is not negligible if the value of ℓ and h is small, especially when LWC/LWC$_a$ > 0.9. Therefore, the subsample with LWC/LWC$_a$ > 0.9 was excluded when calculating DHM(m).

Figure 7a shows the DHM(m) as a function of the subsample length in z coordinate for spatially clustered (RC$_{max}$ > 1) and randomly distributed (RC$_{max}$ < 1) holograms observed near the cloud top. The DHM(m) of spatially clustered

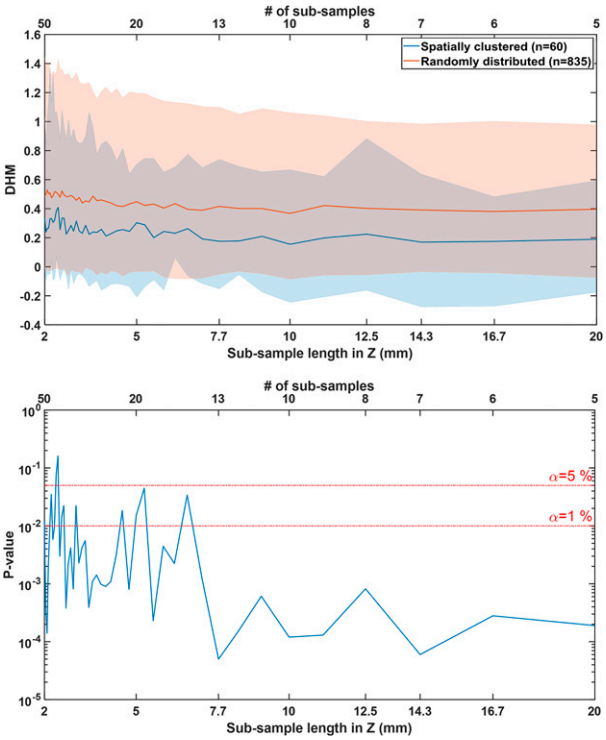

FIG. 7. (a) DHM(m) as a function of subsample length in z coordinates for the clustered (blue) and random (red) holograms observed near the cloud top for RF02. The lines indicate median DHM(m) and the shaded areas represent the spectral width (10th–90th-percentile range) of DHM(m). The numbers in parentheses in the legend indicate the number of clustered and random holograms; and (b) the p values for the permutation hypothesis test as a function of subsample length in z coordinates.

holograms [DHM$_{clu}$(m)] is lower than the DHM(m) of randomly distributed holograms [DHM$_{ran}$(m)]. To evaluate whether the difference in the DHM(m) for the two groups (spatially clustered and randomly distributed holograms) is statistically significant, we conduct a resampling test (known as the permutation test). Under the null hypothesis that the two groups are from the same population, all holograms [835 (random) + 60 (clustered)] are mixed together. Then 60 are selected randomly and these are classified into the clustered distribution group, and the unselected 835 into the random distribution group. Under the null hypothesis, the test statistic of the difference between the median DHM of the randomly selected random group and that of the randomly selected clustered group (i.e., DHM$_{ran}$ − DHM$_{clu}$) is expected to be zero. Such resampling procedure is repeated 100 000 times and each time the test statistic is calculated for each of all m values. These test statistic values for each m constitute the null distribution of DHM$_{ran}$(m) − DHM$_{clu}$(m), which can be compared to the observed test statistic to evaluate the statistical significance. The p value for this permutation hypothesis test is shown in Fig. 7b for each m (shown as a function of subsample length). Since DHM$_{clu}$(m) is expected to be smaller than DHM$_{ran}$(m), this hypothesis test is one-tailed. The p values are mostly

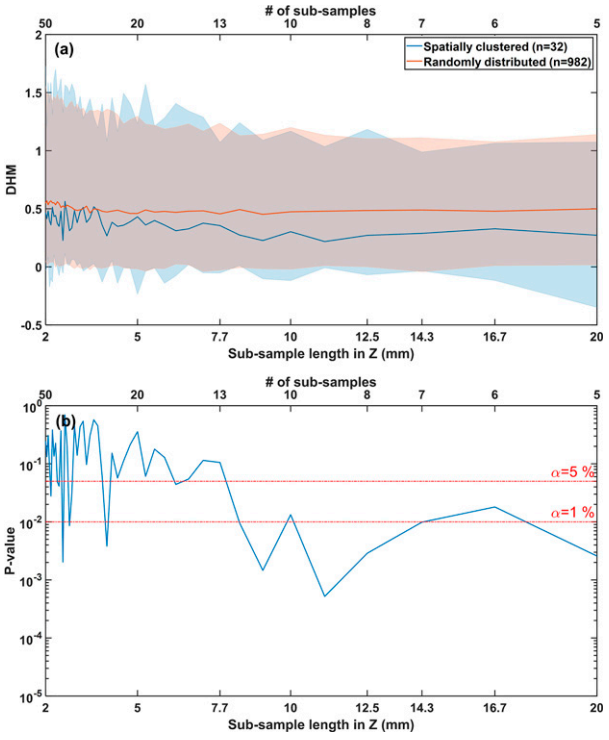

FIG. 8. As in Fig. 7, but for the holograms observed relatively deeper into the cloud.

lower than 5% and even lower than 1% for longer subsample lengths, which indicates that the observed difference of the degree of homogeneous mixing between spatially random and clustered distributions is indeed statistically significant at 5% test level for most subsample lengths and even at 1% test level for longer subsample lengths. In other words, it can be said that spatially clustered holograms show stronger visual traits of inhomogeneous mixing than randomly distributed holograms do. On the other hand, the holograms observed relatively deeper into the cloud (120 m below the cloud top) do not show statistically significant differences between $\mathrm{DHM}_{\mathrm{clu}}(m)$ and $\mathrm{DHM}_{\mathrm{ran}}(m)$ for all subsample lengths except for a few long subsample lengths as shown in Fig. 8.

b. *Degree of homogeneous mixing in the LWC–τ_p diagram*

Second, we quantify the degree of homogeneous mixing, using the new approach proposed by Yeom et al. (2021), which uses the LWC–τ_p diagram to estimate the mixing type, where τ_p is the phase relaxation time:

$$\tau_p = (2\pi D_c N_c \overline{D})^{-1} \tag{5}$$

and

$$\mathrm{LWC} = \frac{\pi}{6}\rho N_c D_v^3, \tag{6}$$

where $\overline{D}$ is the mean diameter of the droplets, ρ is the density of water, and D_c is the molecular diffusion coefficient for water vapor. If N_c decreases but the droplet sizes remain unchanged as in the case of inhomogeneous mixing, the slope (γ_s) in the $\log_{10}(\mathrm{LWC})$ versus $\log_{10}(\tau_p)$ diagram will approach -1 because then LWC and τ_p becomes a function of N_c only and Eqs. (5) and (6) suggest an inverse relationship between LWC and τ_p when $D_v \approx \overline{D}$ is assumed (Yeom et al. 2021). Such assumption is found to be reasonable as $D_v/\overline{D} = 1.04 \pm 0.02$ (independent of subsample length) was found for all inhomogeneous mixing cases ($\gamma_s \approx 1$) in our dataset. Figure 9 shows two examples of an LWC–τ_p diagram. Similar to a mixing diagram, the different RH lines are determined by the heat and moisture balance equations [i.e., Eqs. (3) and (4)]. In Fig. 9a, most of the data points clearly line up with the inhomogeneous line and therefore the slope of the linear regression line (γ_s) is almost identical to this line. It was clearly not the case in Fig. 9b, suggesting deviation from inhomogeneous mixing. We consider that how much different γ_s is from -1 would indicate a degree of homogeneous mixing.

We analyze the γ_s values for the random and clustered distribution groups for each m and they are shown in Fig. 10. Certainly, the holograms with spatially clustered droplet distributions have the γ_s values closer to -1 than those with random distribution for all m values. To evaluate the statistical significance of such differences of γ_s between the random and clustered groups, the permutation test is done in the similar manner as described above. Again permutation resampling is done 100 000 times and the null distributions of the test statistic, $[\text{median } \gamma_s(m)]_{\mathrm{ran}} - [\text{median } \gamma_s(m)]_{\mathrm{clu}}$, are generated for all m values. The p values of the observed test statistic are so low that the null hypothesis (the random and clustered groups are from the same population) is rejected clearly even at 1% test level for all m values, implying that the observed differences of $\gamma_s(m)$ between the random and clustered groups are statistically very significant for the holograms observed near the cloud top. These results also indicate that spatially clustered holograms appear to exhibit stronger traits of inhomogeneous mixing than randomly distributed holograms. On the other hand, Fig. 11 shows that there are much less significant differences between the $\gamma_s(m)$ of clustered and random holograms observed relatively deeper into the cloud. Figures S4 and S5 in Supporting Information compare the traits of inhomogeneous mixing between the random and clustered groups for another research flight (RF10) and they show similar trends to those for RF02 shown in Figs. 7–11.

5. Discussion

a. *Relationship between 3D spatial clustering and traits of inhomogeneous mixing*

It is found that the holograms observed near the cloud top with relatively high confidence for spatial clustering exhibit strong visual trait of inhomogeneous mixing. These findings suggest that spatially clustered holograms observed near the cloud top would be indeed affected by inhomogeneous mixing of entrainment air and cloudy air. Table 1 supports this notion, where D_v is almost identical between the random and clustered groups but $\mathrm{N_c}$ is noticeably smaller for the clustered

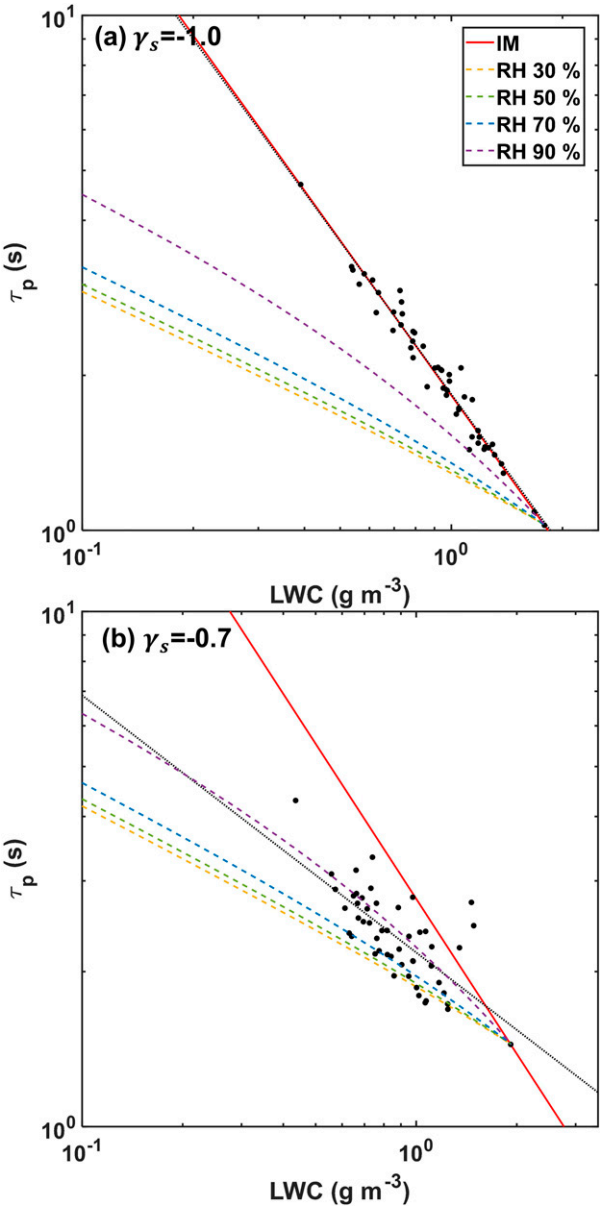

FIG. 9. Examples of a $\log_{10}$(LWC)–$\log_{10}(\tau_p)$ mixing diagram that show the trait of (a) inhomogeneous mixing and of (b) homogeneous mixing. The red line indicates the expected behavior for inhomogeneous mixing, and the dashed lines indicate the expected behavior for homogeneous mixing with the entrained air of given relative humidity. The dotted black straight line represents the linear regression line between $\log_{10}$(LWC) and $\log_{10}(\tau_p)$ and γ_s is the slope of this line. See that in (a) the inhomogeneous mixing line and the regression line are almost identical.

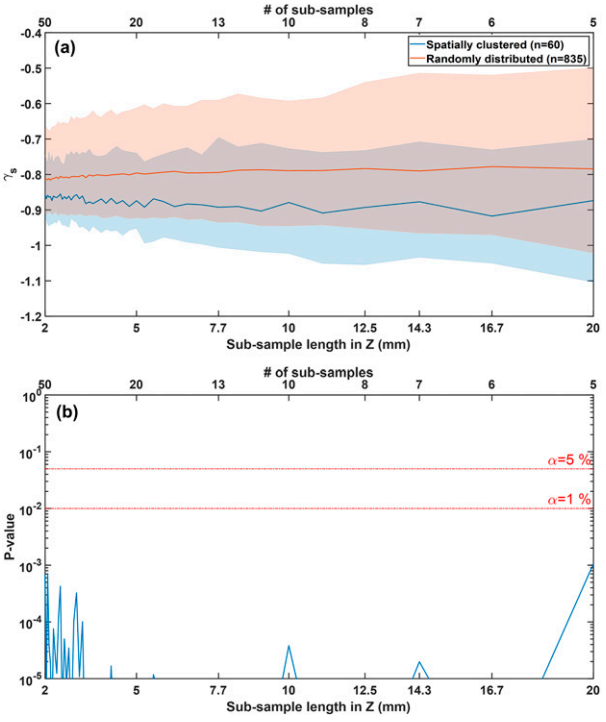

FIG. 10. As in Fig. 7, but for $\gamma_s(m)$.

than for the random group when observed near the cloud top. The reason for showing these distinguishing characteristics between the two groups is likely to be because very dry air is entrained in discrete blobs in the clustered groups as Baker (1992) noted. So, we can speculate that the clustered groups may have been observed in the regions where very dry air blobs are entrained and then mixed with cloudy air inhomogeneously, since the time scale for evaporation of droplets would be short when very dry air is entrained and therefore evaporation could occur nonuniformly. On the other hand, these distinct characteristics between the two groups almost disappear for the holograms observed relatively deeper into the cloud, which will be discussed further in section 5b.

Several studies (e.g., Lu et al. 2014; Gao et al. 2020) investigated the dependence of homogeneous mixing degree on spatial scale. Such investigation is difficult in this study, since we use only a part of the original sample volume of HOLODEC. According to Beals (2013), the uncertainty of D_v increases with the decrease of the number of cloud droplets in the sample volume. Similarly, the uncertainty of the HOLODEC measured V/V_a for RF02 increases as the subsample length decreases, as in Figure S2. This means that the uncertainty of DHM(m) estimation could increase as the subsample length decreases. Furthermore, as shown in Fig. 7, the breath of DHM(m) from their median value increases as the subsample length decreases. On the other hand, $Y_s(m)$ is the slope of a log–log plot, so it would be less affected by the uncertainty of D_v. However, as shown in Fig. 10, the breath of $Y_s(m)$ from their median value increases as m decreases, which indicates that the confidence interval for γ_s increases as m decreases. These results, therefore, need to be interpreted with caution.

b. *The vertical variation of spatial clustering and traits of inhomogeneous mixing*

This study has shown that the holograms with relatively high confidence for spatial clustering are observed more

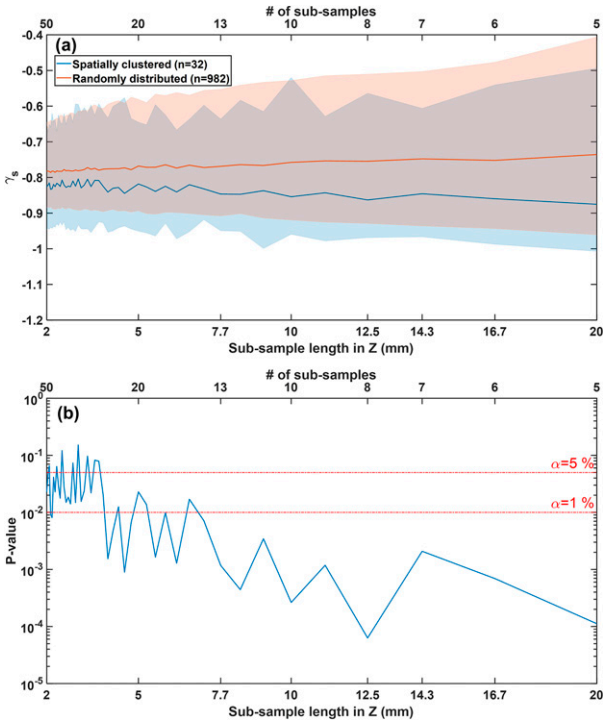

FIG. 11. As in Fig. 10, but for the holograms observed relatively deeper into the cloud.

frequently near cloud top than relatively deeper into the cloud. Previous observational studies (Malinowski et al. 2013; Pedersen et al. 2018) suggested that the thickness of the cloud-top mixing layer containing cloudy air and entrained clear air ranges from 12 to 127 m. That is, the main area directly affected by entrainment and mixing is a portion of the entire cloud layer. Glienke et al. (2020) analyzed the variation of the number of droplets per hologram with the flight distance into the cloud for RF02 analyzed in this study. Diluted holograms were shown at first, but such occurrences were reduced in the middle of horizontal penetrations. As mentioned above, the cloud top height changed during the horizontal penetration in RF02 and the distance from the cloud top was estimated to be at least 120 m for the middle of the horizontal penetration (Fig. 5). That is, the cloud parcels sampled in this section might be less directly affected by entrainment and mixing but relatively well mixed. These results are consistent with that of Dodson and Small Griswold (2019), which showed that the cloud droplets observed with a phase-Doppler interferometer were more clustered toward the edges of cumulus clouds where the immediate effects of entrainment and mixing would likely be evident.

Figure 12 compares the median DHM(m) and $Y_s(m)$ for all holograms in each of the four horizontal penetrations examined in this study (two each from RF02 and RF10). The general trends of decreasing DHM and increasing Y_s are apparent as the subsample length increases (i.e., as m decreases). However, the focus here is the dependence on cloud altitudes. The holograms observed near the cloud top in RF02 exhibit the strongest visual traits of inhomogeneous mixing, showing the lowest DHM and the closest Y_s to -1 regardless of subsample length, among all four penetrations. For the penetration at deeper cloud altitudes, visual traits of inhomogeneous mixing are weakened. For RF10, the differences between the two cloud altitudes are not obvious, perhaps that is because both altitudes (120 and 220 m) are far from where immediate effects of entrainment and mixing would appear. There are also differences between the two flights. For the same cloud altitude of 120 m from the cloud top, RF02 exhibits stronger visual traits of inhomogeneous mixing but we have no clear answer to that at this point. Moreover, Figs. 7–11 and Figure S5 manifest that the statistical significance of the differences of visual traits of inhomogeneous mixing between spatially clustered and random holograms is the strongest near cloud top but it reduces as the distance from the cloud top increases. It means that spatially clustered holograms observed near cloud top could certainly be affected by inhomogeneous mixing, but the effect of inhomogeneous mixing is not apparent even for spatially clustered holograms when observed relatively deeper into the cloud. These results are consistent with the observational studies by Yum et al. (2015) and Yeom et al. (2021) as elaborated in the next paragraph.

Yum et al. (2015) suggested that the mixing of the entrained air near cloud top is dominantly inhomogeneous for the subtropical marine stratocumulus clouds observed off the coast of Chile, but traits of homogeneous mixing became apparent in midlevels of clouds. Since RH would be high in midlevels of clouds, it can be said that this result is consistent with the model simulation of Andrejczuk et al. (2006) that showed that the mixing at high values of RH tended to be homogeneous. However, such vertical variation of mixing traits was also found in Yeom et al. (2021) for the North Atlantic marine stratocumulus clouds. It was argued that such variation was due to vertical circulation mixing (Wang et al. 2009; Yum et al. 2015; Yeom et al. 2021). According to Wang et al. (2009), the vertical circulation mixing mechanism is driven by evaporative and radiative cooling at the cloud top (e.g.,

TABLE 1. Average values of liquid water content (LWC), mean volume diameter (D_v), number concentration (N_c), and relative dispersion ($\sigma/\overline{D}$) for RF02. Here σ is the standard deviation of droplet diameter.

Location	Distribution	LWC (g m^{-3})	D_v (μm)	N_c (cm^{-3})	$\sigma/\overline{D}$
Near cloud top	Clustered	0.40 ± 0.17	14.6 ± 1.4	247 ± 89	0.16 ± 0.03
	Random	0.46 ± 0.13	14.6 ± 1.6	288 ± 72	0.16 ± 0.03
Deeper into the cloud	Clustered	0.64 ± 0.17	16.4 ± 1.6	278 ± 70	0.18 ± 0.04
	Random	0.65 ± 0.12	16.8 ± 1.4	274 ± 57	0.19 ± 0.04

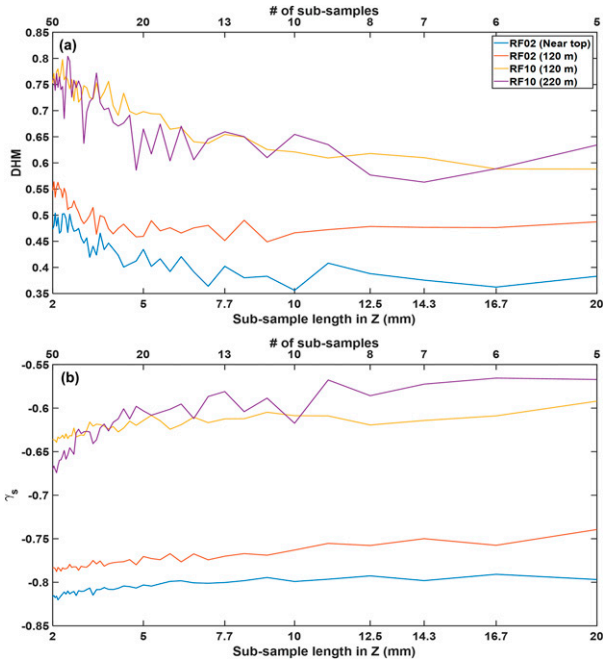

FIG. 12. The median values of (a) DHM and (b) γ_s for all holograms in each of the four horizontal penetrations examined in this study, shown as a function of subsample length in z coordinates. The distances from the cloud top are indicated in parentheses in the legend.

Nicholls 1989; Gerber et al. 2005), which might induce buoyancy reversal that is large enough to satisfy the criterion for cloud-top entrainment instability (CTEI) (Deardorff 1980). Malinowski et al. (2013) similarly argued that once CTEI criterion is satisfied, the mixed parcels in the cloud-top mixing layer could go down to the well-mixed region, if these parcels were not affected by convective circulation. The cloud-top mixing layer can be thicker when CTEI criterion is not satisfied than when CTEI criterion is satisfied, because mixed parcels can remain in the cloud top region when CTEI criterion is not satisfied. Moreover, Yum et al. (2015) and Yeom et al. (2021) showed that vertical variation of mixing traits was found when CTEI criterion was satisfied. We try to calculate CTEI to evaluate whether the clouds we examined here can be subject to vertical circulation. The CTEI criterion proposed by Randall (1980) and Deardorff (1980) is given by

$$\Delta\theta_e - \kappa\left(\frac{L_v}{C_p}\right)\Delta q_t < 0, \tag{8}$$

where Δ indicates jump between the free troposphere and the cloud top. The θ_e and q_t are the equivalent potential temperature $[\theta_e = \theta + (L_v/C_p)q_v]$ and the total water mixing ratio, and the κ is the stability parameter, which would be 0.23 for all cases analyzed in this study (Yamaguchi and Randall 2008). For RF02, the CTEI criterion was indeed satisfied when estimated with the vertical thermodynamic profile observed when the aircraft exited the cloud, but it was not the case when entering the cloud (not shown). For RF10, the closest vertical profile was about 60 km away from the location of cloud exit but it did indicate that CTEI was satisfied. Because of the remoteness of the profile from the clouds, however, it is difficult to have confidence in such estimation. Meanwhile, Katzwinkel et al. (2012) showed that mixing between free-troposphere and the cloudy air near cloud top could be caused not only by buoyancy reversal but also by vertical wind shear. We calculate the gradient Richardson number (Ri) to characterize the growth and decay of turbulence caused by wind shear and atmospheric stability for RF02:

$$\mathrm{Ri} = \frac{g}{\bar{\theta}_l}\frac{\Delta\theta_l}{(\Delta U)^2}\Delta z,$$

where g is the acceleration due to gravity, θ_l the liquid water potential temperature ($\theta_l = \theta - (L_v/C_p)q_l$), and U the horizontal wind velocity. For RF02 wind shear is estimated to be stronger when the CTEI criterion is not satisfied than when satisfied (not shown), and it leads to Ri being smaller where CTEI criterion is not satisfied (~2) than where satisfied (~4), which suggests shear-driven turbulent mixing could play a role in driving mixing when CTEI is not operating. There are significant uncertainties in estimating CTEI and wind shear due to limitations in observing vertical profiles of cloud thermodynamic properties and wind shear near the cloud top region. Moreover, Gerber et al. (2013, 2016) showed evidence that the prediction of CTEI dealing with jumps across entrainment interface layer (EIL) is inaccurate because droplet evaporation primarily cools the EIL, and that radiative cooling dominates entrainment at the base of the EIL. Certainly, there is more work to do in understanding the behavior of the EIL including its partitioning into layers as described by Malinowski et al. (2013) and its effect on the entrainment process and linking microphysical observations to various mechanisms for turbulence production.

6. Summary and conclusions

The HOLODEC data obtained from the Cloud System Evolution in the Trades (CSET) Campaign that was held between Northern California and Hawaii are analyzed to investigate the effects of entrainment and subsequent mixing on droplet spatial structure and droplet spectra at centimeter scales within the observational framework for homogeneous and inhomogeneous mixing. Our main results can be summarized as follows.

With the capability of HOLODEC to discern the 3D structure of cloud droplet distributions, we quantify spatial clustering of droplet distributions using the kth-nearest-neighbor distance. Beals (2013) also quantified spatial clustering using 3D droplet positions recorded by HOLODEC but he did only for the 1st-nearest-neighbor distance to measure spatial clustering. For the hologram data we examine in this study, the spatial distribution of the droplets estimated from the first-nearest-neighbor distance shows no clear difference from the random distribution, even for the holograms that appear to show clustered droplet distribution: the statistical measure of

clustering for the 1st-nearest neighbor, SC(1), is similar to the value found in random distribution. However, spatial clustering of the kth-nearest neighbor, SC(k), is clearly different from that of random distribution, for the k values much greater than 1. That is, spatial clustering varies with k. So the relative clustering, $RC = SC_{obs}/SC_{99.9\%}$, is calculated for each k, and the maximum, RC_{max}, is determined, as an ultimate measure of clustering. The value of k that produces RC_{max} may provide the information on the length scale of spatial n as Baker (1992) argued. That is, it can be said that spatial clustering is maximized at the kth-nearest distance scale that produces RC_{max}. It is found that the average of the kth-nearest distance of RC_{max} for each spatially clustered hologram is approximately 2 cm for RF02. This is consistent with Dodson and Small Griswold (2019), which argued that entrainment mixing could affect spatial clustering at centimeter scale.

Moreover, it is found that RC_{max} tends to be higher for the holograms observed near the cloud top than relatively deeper into the cloud, implying higher confidence for spatial clustering for the holograms near the cloud top. This finding suggests that the immediate effect of entrainment and mixing is to induce spatially clustered droplet distribution patterns. However, spatially clustered holograms are also observed relatively deeper into the cloud, although they are observed less frequently. Perhaps the clustering continues down from the cloud top as the mixed parcels descend. Or it might have been caused by inertial clustering as demonstrated by Larsen et al. (2018) using the 3D radial distribution functions. To note is that in this study small droplets (diameter < 10 μm) are not considered because of the poor detectability of these droplets by HOLODEC. If the concentration of undetected small droplets were significant, the uncertainty in our assessment of spatial clustering might not be negligible. The average N_c from CDP that measured droplets of 2–50 μm diameter range were approximately 300 cm^{-3} for RF02 and 200 cm^{-3} for RF10, respectively, and the concentrations only for 2–10 μm diameter range were 14 cm^{-3} for RF02 and 38 cm^{-3} for RF10, respectively. So the uncertainty due to the neglection of small droplets might be tolerable for RF02 but perhaps not for RF10. Notwithstanding these limitations, such high statistical confidence of spatial clustering for the holograms near the cloud top suggests that including small droplets would not change the test results.

The ultimate question we address is the relationship between spatial clustering and traits of inhomogeneous mixing. We assume that the droplet spatial structure is affected depending on whether the mixing of entrainment air with cloudy air is inhomogeneous or homogeneous. Indeed, the holograms with spatial clustering and those with randomness show clear differences in the visual traits for inhomogeneous mixing: the holograms with spatial clustering show smaller DHM and Y_s than those with random distribution. Such visual traits of inhomogeneous mixing are the strongest for the holograms observed near the cloud top, which is firmly supported by the permutation test. Meanwhile, the visual trait of inhomogeneous mixing is statistically much less significant for the spatially clustered holograms observed relatively deeper into the cloud. So we suggest that the spatially clustered holograms observed near the cloud top indeed experienced inhomogeneous mixing but deeper into the cloud, such traits became much less apparent even for spatially clustered holograms.

These results are consistent with those of Yum et al. (2015) and Yeom et al. (2021), who found that traits of inhomogeneous mixing were strong near cloud top but traits of homogeneous mixing became apparent in midlevels of clouds. They suggested that the mixing of the entrained air near cloud top is dominantly inhomogeneous for subtropical marine stratocumulus clouds, but traits of homogeneous mixing became apparent in midlevels of clouds due to vertical circulation mixing. So it may be the case that the modulation of cloud microphysical parameters during the descent of entrainment affected parcels resulted in the removal of inhomogeneous mixing traits even for spatially clustered holograms. Another thing to note is that the statistical significance of the visual traits of inhomogeneous mixing for spatially clustered holograms increases as the subsample size increases. This is promising because larger subsample size means higher number of droplets being analyzed and therefore greater confidence for statistical evaluations. However, additional data and analyses are necessary to substantiate the results.

Acknowledgments. This work was supported by the National Research Foundation of Korea (NRF) grant funded by the Korea government (MSIT) (Grant NRF-2021R1A2B5B02002458) and the Yonsei Signature Research Cluster Program of 2022-22-0003. R. A. Shaw and J. M. Yeom acknowledge support from U.S. Department of Energy, Office of Science Award DE-SC0020053. We thank S. Glienke (PNNL) and the staff of the NCAR Research Aviation Facility for the effort that went into collecting and processing the HOLODEC data from CSET.

Data availability statement. Field data used in the study are available from the CSET data archive hosted by NCAR http://data.eol.ucar.edu/master_list/?project=CSET.

REFERENCES

Albrecht, B., and Coauthors, 2019: Cloud System Evolution in the Trades (CSET): Following the evolution of boundary layer cloud systems with the NSF–NCAR GV. *Bull. Amer. Meteor. Soc.*, **100**, 93–121, https://doi.org/10.1175/BAMS-D-17-0180.1.

Andrejczuk, M., W. W. Grabowski, S. P. Malinowski, and P. K. Smolarkiewicz, 2006: Numerical simulation of cloud–clear air interfacial mixing: Effects on cloud microphysics. *J. Atmos. Sci.*, **63**, 3204–3225, https://doi.org/10.1175/JAS3813.1.

Baker, B. A., 1992: Turbulent entrainment and mixing in clouds: A new observational approach. *J. Atmos. Sci.*, **49**, 387–404, https://doi.org/10.1175/1520-0469(1992)049<0387:TEAMIC>2.0.CO;2.

Baker, M. B., R. G. Corbin, and J. Latham, 1980: The influence of entrainment on the evolution of cloud droplet spectra: I. A model of inhomogeneous mixing. *Quart. J. Roy. Meteor. Soc.*, **106**, 581–598, https://doi.org/10.1002/qj.49710644914.

Beals, M. J., 2013: Investigations of cloud microphysical response to mixing using digital holography. Ph.D. dissertation, Michigan Technological University, 146 pp.

——, J. P. Fugal, R. A. Shaw, J. Lu, S. M. Spuler, and J. L. Stith, 2015: Holographic measurements of inhomogeneous cloud mixing at the centimeter scale. *Science*, **350**, 87–90, https://doi.org/10.1126/science.aab0751.

Burnet, F., and J.-L. Brenguier, 2007: Observational study of the entrainment-mixing process in warm convective clouds. *J. Atmos. Sci.*, **64**, 1995–2011, https://doi.org/10.1175/JAS3928.1.

Deardorff, J. W., 1980: Cloud top entrainment instability. *J. Atmos. Sci.*, **37**, 131–147, https://doi.org/10.1175/1520-0469(1980)037<0131:CTEI>2.0.CO;2.

Desai, N., S. Glienke, J. Fugal, and R. A. Shaw, 2019: Search for microphysical signatures of stochastic condensation in marine boundary layer clouds using airborne digital holography. *J. Geophys. Res. Atmos.*, **124**, 2739–2752, https://doi.org/10.1029/2018JD029033.

Devenish, B. J., and Coauthors, 2012: Droplet growth in warm turbulent clouds. *Quart. J. Roy. Meteor. Soc.*, **138**, 1401–1429, https://doi.org/10.1002/qj.1897.

Dodson, D. S., and J. D. Small Griswold, 2019: Droplet inhomogeneity in shallow cumuli: The effects of in-cloud location and aerosol number concentration. *Atmos. Chem. Phys.*, **19**, 7297–7317, https://doi.org/10.5194/acp-19-7297-2019.

Gao, S., C. Lu, Y. Liu, F. Mei, J. Wang, L. Zhu, and S. Yan, 2020: Contrasting scale dependence of entrainment-mixing mechanisms in stratocumulus clouds. *Geophys. Res. Lett.*, **47**, e2020GL086970, https://doi.org/10.1029/2020GL086970.

Gerber, H., G. Frick, S. P. Malinowski, J.-L. Brenguier, and F. Burnet, 2005: Holes and entrainment in stratocumulus. *J. Atmos. Sci.*, **62**, 443–459, https://doi.org/10.1175/JAS-3399.1.

——, ——, ——, H. Jonsson, D. Khelif, and S. K. Krueger, 2013: Entrainment rates and microphysics in POST stratocumulus. *J. Geophys. Res. Atmos.*, **118**, 12 094–12 109, https://doi.org/10.1002/jgrd.50878.

——, S. P. Malinowski, and H. Jonsson, 2016: Evaporative and radiative cooling in POST stratocumulus. *J. Atmos. Sci.*, **73**, 3877–3884, https://doi.org/10.1175/JAS-D-16-0023.1.

Glienke, S., A. Kostinski, J. Fugal, R. A. Shaw, S. Borrmann, and J. Stith, 2017: Cloud droplets to drizzle: Contribution of transition drops to microphysical and optical properties of marine stratocumulus clouds. *Geophys. Res. Lett.*, **44**, 8002–8010, https://doi.org/10.1002/2017GL074430.

——, ——, R. A. Shaw, M. L. Larsen, J. P. Fugal, O. Schlenczek, and S. Borrmann, 2020: Holographic observations of centimeter-scale non-uniformities within marine stratocumulus clouds. *J. Atmos. Sci.*, **77**, 499–512, https://doi.org/10.1175/JAS-D-19-0164.1.

Grabowski, W. W., and L.-P. Wang, 2009: Diffusional and accretional growth of water drops in a rising adiabatic parcel: Effects of the turbulent collision kernel. *Atmos. Chem. Phys.*, **9**, 2335–2353, https://doi.org/10.5194/acp-9-2335-2009.

Hoffmann, F., T. Yamaguchi, and G. Feingold, 2019: Inhomogeneous mixing in Lagrangian cloud models: Effects on the production of precipitation embryos. *J. Atmos. Sci.*, **76**, 113–133, https://doi.org/10.1175/JAS-D-18-0087.1.

Jonas, P. R., 1996: Turbulence and cloud microphysics. *Atmos. Res.*, **40**, 283–306, https://doi.org/10.1016/0169-8095(95)00035-6.

Katzwinkel, J., H. Siebert, and R. A. Shaw, 2012: Observation of a self-limiting, shear-induced turbulent inversion layer above marine stratocumulus. *Bound.-Layer Meteor.*, **145**, 131–143, https://doi.org/10.1007/s10546-011-9683-4.

Larsen, M. L., R. A. Shaw, A. B. Kostinski, and S. Glienke, 2018: Fine-scale droplet clustering in atmospheric clouds: 3D radial distribution function from airborne digital holography. *Phys. Rev. Lett.*, **121**, 204501, https://doi.org/10.1103/PhysRevLett.121.204501.

Lehmann, K., H. Siebert, and R. A. Shaw, 2009: Homogeneous and inhomogeneous mixing in cumulus clouds: Dependence on local turbulence structure. *J. Atmos. Sci.*, **66**, 3641–3659, https://doi.org/10.1175/2009JAS3012.1.

Lu, C., Y. Liu, and S. Niu, 2011: Examination of turbulent entrainment-mixing mechanisms using a combined approach. *J. Geophys. Res. Atmos.*, **116**, D20207, https://doi.org/10.1029/2011JD015944.

——, ——, ——, and S. Endo, 2014: Scale dependence of entrainment-mixing mechanisms in cumulus clouds. *J. Geophys. Res. Atmos.*, **119**, 13 877–13 890, https://doi.org/10.1002/2014JD022265.

——, and Coauthors, 2020: Reconciling contrasting relationships between relative dispersion and volume-mean radius of cloud droplet size distributions. *J. Geophys. Res. Atmos.*, **125**, e2019JD031868, https://doi.org/10.1029/2019JD031868.

Malinowski, S. P., and Coauthors, 2013: Physics of Stratocumulus Top (POST): Turbulent mixing across capping inversion. *Atmos. Chem. Phys.*, **13**, 12 171–12 186, https://doi.org/10.5194/acp-13-12171-2013.

McGraw, R., and Y. Liu, 2004: Analytic formulation and parametrization of the kinetic potential theory for drizzle formation. *Phys. Rev. E*, **70**, 031606, https://doi.org/10.1103/PhysRevE.70.031606.

Nicholls, S., 1989: The structure of radiatively driven convection in stratocumulus. *Quart. J. Roy. Meteor. Soc.*, **115**, 487–511, https://doi.org/10.1002/qj.49711548704.

Pawlowska, H., J. L. Brenguier, and F. Burnet, 2000: Microphysical properties of stratocumulus clouds. *Atmos. Res.*, **55**, 15–33, https://doi.org/10.1016/S0169-8095(00)00054-5.

Pedersen, J. G., Y.-F. Ma, W. W. Grabowski, and S. P. Malinowski, 2018: Anisotropy of observed and simulated turbulence in marine stratocumulus. *J. Adv. Model. Earth Syst.*, **10**, 500–515, https://doi.org/10.1002/2017MS001140.

Pruppacher, H. R., and J. D. Klett, 1997: *Microphysics of Clouds and Precipitation.* Atmospheric and Oceanographic Sciences Library, Vol. 18, Springer, 954 pp.

Randall, D. A., 1980: Conditional instability of the first kind up-side down. *J. Atmos. Sci.*, **37**, 125–130, https://doi.org/10.1175/1520-0469(1980)037<0125:CIOTFK>2.0.CO;2.

Rogers, R. R., and M. K. Yau, 1989: *A Short Course in Cloud Microphysics.* 3rd ed. Pergamon Press, 293 pp.

Shaw, R. A., 2003: Particle-turbulence interactions in atmospheric clouds. *Annu. Rev. Fluid Mech.*, **35**, 183–227, https://doi.org/10.1146/annurev.fluid.35.101101.161125.

——, A. B. Kostinski, and M. L. Larsen, 2002: Towards quantifying droplet clustering in clouds. *Quart. J. Roy. Meteor. Soc.*, **128**, 1043–1057, https://doi.org/10.1256/003590002320373193.

Uhlig, E. M., S. Borrmann, and R. Jaenicke, 1998: Holographic in-situ measurements of the spatial droplet distribution in stratiform clouds. *Tellus*, **50**, 377–387, https://doi.org/10.3402/tellusb.v50i4.16210.

Vaillancourt, P. A., and M. K. Yau, 2000: Review of particle–turbulence interactions and consequences for cloud physics. *Bull. Amer. Meteor. Soc.*, **81**, 285–298, https://doi.org/10.1175/1520-0477(2000)081<0285:ROPIAC>2.3.CO;2.

Wang, J., P. H. Daum, S. S. Yum, Y. Liu, G. I. Senum, M. L. Lu, J. H. Seinfeld, and H. Jonsson, 2009: Observations of marine stratocumulus microphysics and implications for processes controlling droplet spectra: Results from the marine stratus/

stratocumulus experiment. *J. Geophys. Res. Atmos.*, **114**, D18210, https://doi.org/10.1029/2008JD011035.

Warner, J., 1973: The microstructure of cumulus cloud: Part IV. The effect on the droplet spectrum of mixing between cloud and environment. *J. Atmos. Sci.*, **30**, 256–261, https://doi.org/10.1175/1520-0469(1973)030<0256:TMOCCP>2.0.CO;2.

Yamaguchi, T., and D. A. Randall, 2008: Large-eddy simulation of evaporatively driven entrainment in cloud-topped mixed layers. *J. Atmos. Sci.*, **65**, 1481–1504, https://doi.org/10.1175/2007JAS2438.1.

Yang, F., R. Shaw, and H. Xue, 2016: Conditions for superadiabatic droplet growth after entrainment mixing. *Atmos. Chem. Phys.*, **16**, 9421–9433, https://doi.org/10.5194/acp-16-9421-2016.

Yeom, J. M., S. S. Yum, Y. Liu, and C. Lu, 2017: A study on the entrainment and mixing process in the continental stratocumulus clouds measured during the RACORO campaign. *Atmos. Res.*, **194**, 89–99, https://doi.org/10.1016/j.atmosres.2017.04.028.

——, ——, F. Mei, B. Schmid, J. Comstock, L. A. T. Machado, and M. A. Cecchini, 2019: Impact of secondary droplet activation on the contrasting cloud microphysical relationships during the wet and dry seasons in the Amazon. *Atmos. Res.*, **230**, 104648, https://doi.org/10.1016/j.atmosres.2019.104648.

——, and Coauthors, 2021: Vertical variations of cloud microphysical relationships in marine stratocumulus clouds observed during the ACE-ENA campaign. *J. Geophys. Res. Atmos.*, **126**, e2021JD034700, https://doi.org/10.1029/2021JD034700.

Yum, S. S., and J. G. Hudson, 2001: Microphysical relationships in warm clouds. *Atmos. Res.*, **57**, 81–104, https://doi.org/10.1016/S0169-8095(00)00099-5.

——, J. Wang, Y. Liu, G. Senum, S. Springston, R. McGraw, and J. M. Yeom, 2015: Cloud microphysical relationships and their implication on entrainment and mixing mechanism for the stratocumulus clouds measured during the VOCALS project. *J. Geophys. Res. Atmos.*, **120**, 5047–5069, https://doi.org/10.1002/2014JD022802.